Cluster Formation in Liquid Lithium Niobate A Small Angle X-ray Scattering Investigation

P. Andonov[a], S. Kimura[b], T. Sawada[b], and A. Kobayashi[c]

[a] Laboratoire de Magnétisme et d'Optique de l'Université de Versailles 1, place Aristide Briand
CNRS-Bellevue, 92195 Meudon CEDEX France
[b] National Institute for Research in Inorganic Materials (NIRIM), I-I Namiki,
Tsukuba-shi Ibaraki, 305 Japan
[c] National Laborarory for High Energy Physics (KEK), I-I Oho, Tsukuba-shi Ibaraki, 305 Japan

Z. Naturforsch. **51a**, 133–146 (1996); received December 27, 1995

Structural analysis of the clustering phenomenon in the $LiNbO_3$ melt was carried out by means of small-angle X-ray scattering using synchrotron radiation in the range of momentum transfer $0.2\ \text{nm}^{-1} \leq k \leq 14.0\ \text{nm}^{-1}$. Microclusters were present in the melt throughout the entire explored temperature-domain from 1673 K to 1513 K which includes undercooling (melting point $T_m = 1526$ K). The radius of gyration, size, shape and distance of particles were determined. Chains of few NbO_6 octahedra and small blocks constituted by two layers of four corner-shared octahedra, interlocked by a lithium atom, could be good models for the microclusters in a large temperature-domain. By lowering the temperature, the particle size increased. Below 1553 K, probable macroclusters would be correlated to the rapid increase of the viscosity. Using the viscosity data and previously published and the present SAXS results, it was possible to evaluate the volume of the clusters. Near the freezing point about a quarter of the volume would be occupied by clusters.

Indexing codes: 61.60.Lx experimental diffraction and scattering techniques; 61.25.Ks molten salts; 36.40.+d atomic and molecular clusters.

Introduction

A characteristic behaviour of an expanding fluid has been detected in molten lithium niobate on cooling between 1590 K and 1560 K, and a marked increase of the viscosity was always observed below 1553 K [1–3]. These observations implied a strong modification in the liquid local and medium range ordering. This behaviour, near the melting point T_m, might be correlated with the appearance of subgrain boundaries [4, 5] affecting the crystal growth since the single crystals are synthesized from the melt by the pulling method of Czochralski [6]. The Nb coordination in the melt has recently been determined from structural studies carried out by high temperature X-ray and neutron diffraction [7, 8]. These results confirm a local ordering in the melt similar to the crystalline one up to the highest explored temperature with a persistent octahedral Nb coordination as observed in the crystal, which is classified in the family of ilmenite. In its ferroelectric phase, the crystal belongs to the rhombohedral system with the space group R3c [9]. A Li atom is trapped in a framework of eight octahedra of O atoms with the heavy Nb atom located in each octahedron (see Figure 1 a). It has been proposed that the space group becomes $R\bar{3}$ or $R\bar{3}c$ [9, 10] at the Curie point, T_c, just a few degrees below T_m. With Nb midway between nearest oxygen layers and Li in the oxygen layer at c/4 from Nb, the Nb position acquires the symmetry of an inversion center in this phase (see Figure 1 b). From these results it may be imagined that clusters are present in the melt and a possible rearrangement could appear for some of them near the freezing point. To confirm this assumption, we present structural information obtained using Small Angle X-ray Scattering (SAXS). The paper is organized as follows. After some background on SAXS and on the methods chosen for the data analysis (Part II), the data correction, normalization and accuracy are presented in Part III. The experiments are described in Part IV, and the results are reported in Part V. A discussion of the microcluster model and of the cluster evolution with temperature follows in Section VI.

Reprint requests to Prof. P. Andonov.

0932-0784 / 96 / 0300-0133 $ 06.00 © – Verlag der Zeitschrift für Naturforschung, D-72072 Tübingen

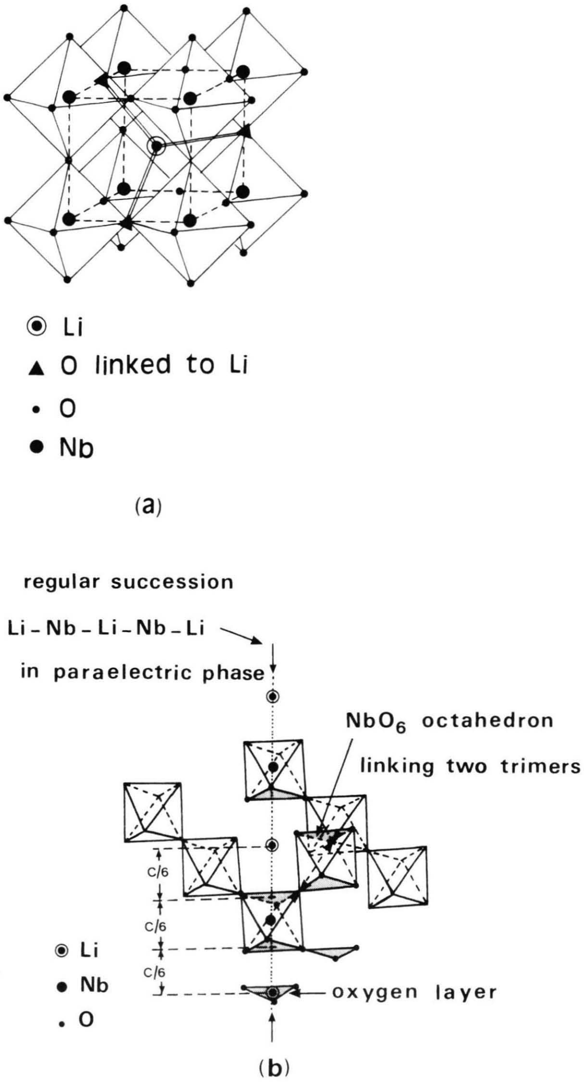

Fig. 1. Models of the crystalline structure. a) regular framework of eight octahedra of oxygen atoms. b) regular succession of Li and Nb atoms in the paraelectric phase.

1. Small Angle X-ray Scattering

1.1. Background

SAXS is observed when electron density fluctuations exist in the melt and if these inhomogeneities can be assumed to be continuous. The scattering intensity (expressed in cm^{-1}) is given by

$$I_T(k)=N\Big[\sum_i A_i^2(k)\cdot f(a_i)+\sum\sum_{i\neq j} A_i(k)\cdot A_j(k)\cdot f(a_i)\cdot f(a_j)\cdot\{S_{ij}(k,d)-1\}\Big]+I_p, \quad (1)$$

where N is the total particle number density and d the distance between the particles with diameters a_i and scattering amplitudes $A_i(k)$. The wave vector k is equal to $4\pi\sin\Theta/\lambda$ (where 2Θ is the scattering angle and λ the wavelength). The distribution functions of particles i and j are respectively $f(a_i)$ and $f(a_j)$; $S_{ij}(k,d)$ is their pair structure function. The summation is over the scattering volume. For spherical particles with internal uniform electron density ϱ_p, dispersed in a surrounding medium of constant density ϱ_0, the scattering amplitude $A_i(k)$ is proportional to the contrast $\Delta\varrho=(\varrho_p-\varrho_0)$. For non-spherical particles, spheres equivalent to the scattering volume of real particles can be considered with the mean values $\langle A_i^2(k)\rangle$ and $\langle A_i(k)\rangle^2$, averaged again over all the possible orientations of the real particles with respect to the wave vector. I_p is the scattering part, non-sensitive to the structure. Several cases can be distinguished for the scattering behaviour.

i) If N widely separated identical particles are present in the medium, the structure sensitive intensity, $I(k)$, is N times the intensity scattered by a single particle $i(k)$, given by Guinier [11] as

$$i(k)=n^2\cdot\exp\left\{\frac{-4\pi s^2 R_g^2}{3}\right\}$$

$$\text{with } s=k/2\pi \quad\text{and}\quad I(k)=N\cdot i(k), \quad (2)$$

where R_g is the radius of gyration of the particle and n the total number of electrons in a particle.

ii) When $k\gg 1/R_g$, i.e. at high angles, the tail of $I(k)$ is expressed by Porod's law [12] and is proportional to the total surface area of the particles, S, in the scattering volume:

$$I(k)\approx I_e(k)\,\frac{2\pi(\Delta\varrho)^2 S}{k^4} \quad (3)$$

with $I_e(k)$ the intensity diffracted by one electron.

(iii) If the identical particles are closer packed, the intensity depends on their distribution, and in this case interparticle interference is often observed in the intermediate k-region where a relative maximum appears.

These three regions are distinguishable and indexed in the present text by {1} near the origin, {2} in the intermediate domain and {3} at high angles.

When non-identical particles are closely packed in the medium, the characteristic scattering function of these particles is determined by the Fourier transform (FT) of $I(k)$, but no simple method is known to extract from this function, simultaneously, the size and shape of the particles. We have assumed that the particles have standard shapes of revolution for which the $A_i(k)$ are tabulated [11–13]. A theoretical intensity is thus computed and compared to the experimental $I(k)$. The global $S(k, d)$ function is determined either by combining these SAXS data with the results obtained by high temperature diffraction [7], or completing these SAXS data at high k by means of models (the intensity is calculated from the Percus Yevick model [14] considering the melt as a medium containing a dense spatial arrangement of nearly spherical clusters).

1.2. Data Analysis

A first and rapid analysis was obtained assuming uncoupled k-regions and using $I(k)$ evaluated in relative units. The region $\{1\}$ is studied in terms of scattering from well separated identical macroclusters for which R_g is deduced from the Guinier approximation [11]. Near the origin, the slope of a $\ln I(k)$ versus k^2 plot gives the R_g value which can be related to the particle dimensions regardless of shape. This method is applied for identical particles without preferential orientations when R_g satisfies $k_{\min} \leq 1/R_g$. The region $\{2\}$ is interpreted in terms of scattering from numerous small particles. Their mean size and their average distance are given by $\{\text{“}a\text{”} \propto \Delta k^{-1}\}$ and $\{\bar{d} \propto k_m^{-1}\}$, where Δk^{-1} is the angular width of the ring of diffraction and k_m is the position of its maximum. The distance $\bar{d}$ is estimated using the Ehrenfest method [15]

$$2\,\bar{d} \sin \Theta_m = 1.23\,\lambda \quad \text{or} \quad \bar{d} = 2.46\,\pi/k_m \tag{4}$$

with $2\,\Theta_m$ the scattering angle for the maximum. An arithmetic mean, R_{0m}, of the radii of gyration of these small particles has been calculated by the method of Hosemann [16]. When the curve $k^2 I(k)$ presents a well-defined maximum, the tangent at the inflexion point, on the high angle side of the ring, intersects the k axis at the position k_t, and R_{0m} is found by the relation

$$R_{0m} = \frac{1}{k_m} \sqrt{\frac{6}{n+2} \frac{\Gamma \frac{n+2}{2}}{\Gamma \frac{n+1}{2}}} \quad \text{with} \quad \frac{k_t}{2\,k_m} - 1 \approx \frac{1}{\sqrt{2(n+1)}}. \tag{5}$$

The region $\{3\}$ is exploited using the asymptotic method of Porod [12]. This method is valid for particles of arbitrary shape, distributed arbitrarily in a homogeneous medium only if $k^4 \cdot I(k)$ is constant over a sufficient k-interval. In this case the absolute specific surface per unit volume, S_{sp}, is given by

$$S_{sp} = \frac{\lim\{k^4 \cdot I(k)\}}{V \cdot 2\pi (\Delta\varrho)^2\, I_e(k)} = \pi\, c(1-c) \frac{\lim\{k^4 \cdot I(k)\}}{\int_0^\infty k^2\, I(k)\, dk} \tag{6}$$

with the normalization condition

$$\int_0^\infty k^2\, I(k)\, dk = 2\,\pi^2\, I_e(k)\, (\Delta\varrho)^2\, Vc(1-c) \tag{7}$$

and Vc the volume fraction occupied by the particles. According to Porod [12], some relations exist between the particle parameters and the limiting values such as: $\{I(k)\}_{k\to 0}$, $\{I(k) \cdot k\}_{k\to 0}$ and $\{I(k) \cdot k^2\}_{k\to 0}$. These determinations are sensitive to extrapolation to zero angle and therefore subject to error, but they give access to simple physical parameters which are useful, in this work, for the discrimination between various models. The correlation length l_c and the range of inhomogeneity l_0 have been defined in terms of the average length l, using the Porod relations as follows:

$$l_c = \frac{\int_0^\infty k\, I(k)\, dk}{\int_0^\infty k^2\, I(k)\, dk} \approx \overline{l^2}/\bar{l} \quad \text{and} \quad l_0 \approx \bar{l} \approx \frac{4\,Vc}{S}. \tag{8}$$

The separation of the $I(k)$ curves in three well-defined regions is also subject to criticism since the different scattering laws are superimposed in the whole k-domain. However any structural change in progress in the melt will be immediately revealed by the temperature dependence of the parameters obtained from this analysis.

After this preliminary treatment, the results are analyzed in real space using the distance distribution function , $p(r)$, given by the (FT) of $I(k)$ as

$$p(r) = \frac{1}{2\,\pi^2} \int_0^{k_{\max}} I(k)\, k\, r \sin(k\, r)\, dk, \tag{9}$$

where $I(k)$ has to be normalized in electron units. With our data analysis, the influence of any left over background correction on the final result is negligible. However, Fourier ripples are present and are caused by termination errors due to the limited value of $k_{\max}$. An artificial extension of the curves $I(k)$ to higher k values permitted us to obtain real space patterns that represent the size and the shape of the particles within reasonable approximation (see paragraph V).

2. Data Corrections

2.1. Background

To obtain the coherent intensity $I(k)$, the only one related to the particle distribution, the non structure sensitive part of the intensity, I_p, has to be subtracted from I_T. This part is the sum of several terms: incoherent scattering I_{inc}, multiple scattering I_{ms}, thermal scattering I_{th}, air scattering I_{air} and parasitic background I_b. The incoherent and multiple scattering were evaluated from the ratios I_{inc}/I_{eu} and I_{ms}/I_{eu} in which I_{eu} is the theoretical coherent intensity expressed in electron units. These ratios were computed using: 1.) the scattering factors given by the analytic expression of Cromer and Waber [17], 2.) the dispersion corrections $\Delta f'$ and $\Delta f''$ reported by Cromer [18], 3.) the tables for X-ray Crystallography [19]; and 4.) the atomic incoherent intensities tabulated by Sagel [20].

Only the double scattering, I_{d2}, is considered in this work since it is the major contribution to I_{ms}. The ratio, I_{d2}/I_{eu}, was calculated by the Warren method [21] and by the method of Malet et al. [22] applied to a transmission geometry and a polarized incident beam. This ratio is computed correlating I_{d2} with the experimental intensity measured from high angle diffraction [7] and using the atomic absorption coefficient $\mu = 182.6$ corresponding to a wavelength $\lambda = 0.12$ nm (reflection on one Si(111) crystal, under the incidence angle $\alpha = 11.02°$), a sample thickness of $h = 10^{-2}$ cm and the temperature T_m. These methods give weak deviations which are without great effect since I_{d2} is always smaller than 0.65% I_{eu}.

The total amplitude of the $\{(I_{inc} + I_{d2})/I_{eu}\}$ correction reaches 1.4% in the worst case.

Thermal scattering is not easy to estimate in a disordered material. If the defect number is low enough to not modify the thermal fluctuations, and with the assumption that the medium is isotropic and that only the longitudinal waves contribute to SAXS, the thermal intensity is given by

$$I_{th} = \frac{f^2}{m} \frac{k_B T}{V_L^2}, \tag{10}$$

where m is the mean atomic mass, f the scattering factor of the mean atom [21] (defined from the composition by $f = 0.2\, f_{Li} + 0.2\, f_{Nb} + 0.6\, f_O$), k_B is the Boltzmann's constant and T the absolute temperature. In an anisotropic medium the longitudinal sound velocity, V_L, has to be replaced by the mean value, V_m, computed from the elastic coefficients [23]. A verification of the procedure was obtained from the intensities scattered by a $LiNbO_3$ monocrystal at 300, 673, 1073 and 1243 K using V_m values (for instance at 300 K with the value $V_m = 5.6 \times 10^5$ cm · s^{-1} we obtain $I_{th(300)} \approx 0.16 \pm 0.02$ electrons/mean atom). A similar evolution was assumed in the liquid, and I_{th} was evaluated by extrapolation to obtain

$I_{th(1523)} = 1.2 \pm 0.2$ and

$I_{th(1673)} = 1.4 \pm 0.2$ electrons/mean atom.

Air scattering is the most important parasitic term because the beam path in air cannot be suppressed near the furnace. Its value can be computed if the air density, d_{air}, is known along the X-ray path. An exponential decay of the air temperature, T_{air}, is assumed versus the distance x away from the centre of the furnace along the incident X-ray direction. A good approximation of T_{air} is obtained by

$$T_{air} = 2^n\, \Gamma(0.5\, n + 1)\, i^n \operatorname{erfc}(x), \quad \text{where}$$

$$\operatorname{erfc}(x) = \frac{2}{\sqrt{\pi}} e^{-x^2}\, dx \tag{11}$$

with $n = 22$ and the integral values reported by Abramowitz [24]. The air density is estimated from

$$d_{air} = \frac{0.001293}{1 + 0.00367\, T_{air}}. \tag{12}$$

I_{air} was evaluated using this assumption for the short beam paths in air at atmospheric pressure (one constituted by 15 mm at room temperature near the detector window; two others, 85 mm plus 105 mm, at variable temperature on either side of the furnace). This evaluation was experimentally verified from the intensities measured with the empty furnace at 300, 900 and 1623 K (Figure 2 a–b).

The final background correction of I_b was made according to Porod [12] or Luzzati [25] from the slope of the plot $I \cdot k$ versus k^3.

2.2. Normalization

In our experiments the primary intensity has not been directly measured from a standard. Only indirect methods could be used. The first normalization factor was obtained by a comparison of the computed values I_{d2} and I_{th} with the intensities scattered by a mono-

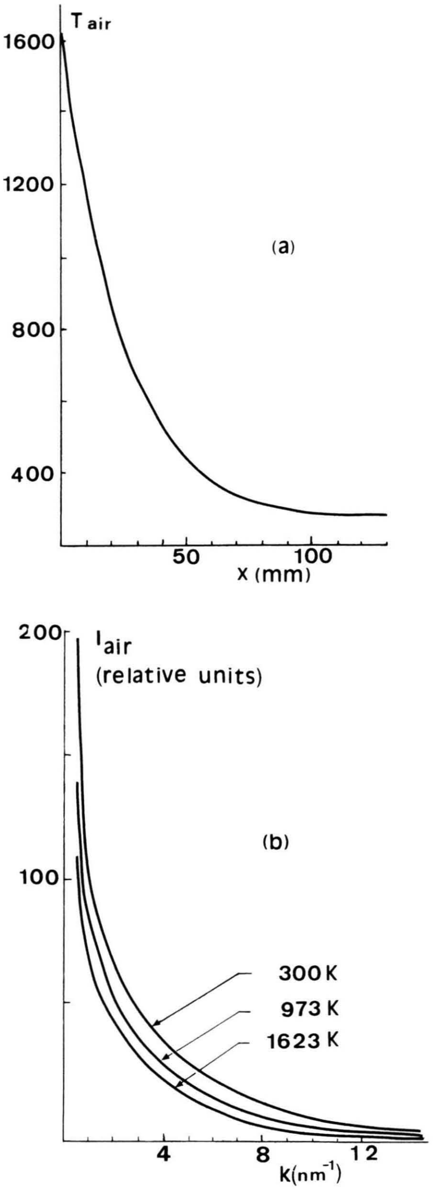

Fig. 2. Evaluation of the air scattering. a) $T_{air}(x)$; air temperature as a function of the distance from the furnace when the empty furnace is stabilized at 1623 K; (T expressed in degrees K). x is the distance from the centre of the furnace. b) $I_{air}(k)$; air scattering measured when the empty furnace is stabilized at 300 K, 973 K and 1623 K.

crystal at several temperatures. The second evaluation was made from the overlap of the termination of the SAXS curves with the low k-range of the normalized patterns given by high temperature diffraction [7]. An agreement between both methods is observed with a discrepancy of 20%. For a counting time of 1000 s, a sample volume of 2.25×10^{-2} cm^3 and the value of the incident synchrotron beam of 200 mA, we had

K_N for 1 count ≈ 0.02 electrons per mean atom
or ≈ $(78 \pm 8) \times 10^{17}$ electrons/cm^3.

3. Experiment

3.1. Sample Environment

An original furnace was designed to maintain at constant temperature a thin liquid specimen in a vertical position without any container. A 0.5 mm diameter platinum wire, shaped into three rings connected in series, is the heating element (see Figure 3a). The central ring keeps the solid disk shaped specimen which becomes a liquid film at high temperature. The two terminal rings are connected to electrodes which feed an electrical current; their action is also to reduce the deformation of the central ring due to thermal expansion. The current was regulated by means of a PID controlled thyristor, and the signal for control was supplied by a 0.1 mm Pt-Rh thermocouple put in the central ring, but aside of the beam path. The melt temperature was obtained on the basis of a preparatory calibration to check the ΔT gradient between the center of the ring and the position of the control thermocouple. The stability was within $\pm 5°$. The heater is in a glass box whose top and bottom are made of a cooling water jacket. Along the beam path, holes in the glass windows let incident and scattered X-rays pass without obstacle. The sample film faces were not really parallel across the whole ring area (see Fig. 3b), the cross section of the beam had to be limited to small dimensions ($\leq 1.2 \times 1.2$ mm^2). Another difficulty was the variation of the sample absorption due to non-negligible evaporation during the experiment. For each scattering temperature the absorption of the sample was measured before and after counting, and the mean absorption factor was evaluated giving an independent check of the evaporation rate. But the short counting time, chosen to reduce this evaporation, gives a statistical error reaching ≈10% in the worst cases. The furnace was installed on the X-ray equipment BL-10C, at the synchrotron source in Tsukuba. The collimation of the incident beam, its small size and its weak divergence with narrow slits (height = width ≤ 1.2 mm) permit us to assume a quasi pin-hole collimation in this SAXS transmission geom-

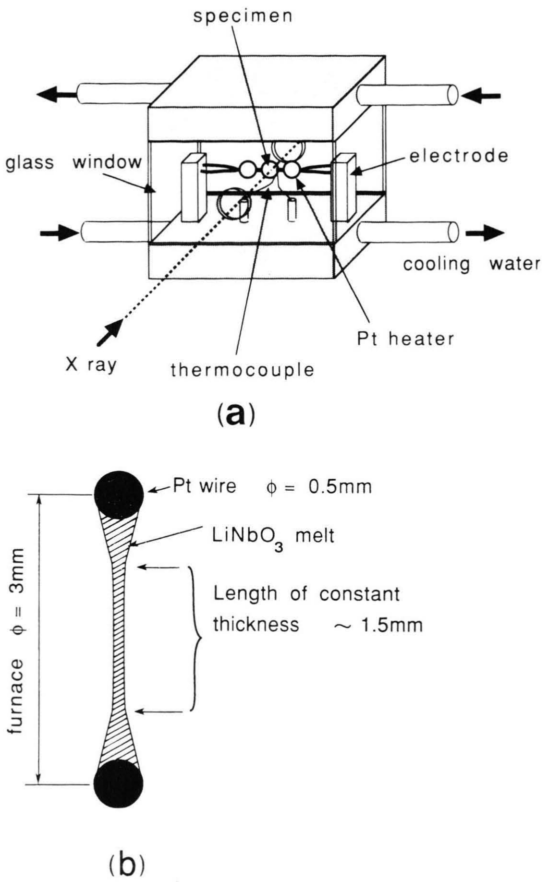

Fig. 3. Furnace design. a) original miniature furnace built for the SAXS study of $LiNbO_3$ melt. b) section of the liquid sample.

etry. The wavelength value was controlled from the sixth order reflections of the reference collagen sample ($\lambda = 0.120 \pm 0.0001$ nm). With the limits imposed by the vacuum pipes, the direct beam stopper and the distance detector-sample (530 mm), the total scattering vector domain explored was $0.20\ \mathrm{mm}^{-1} \leq k \leq 14.00\ \mathrm{nm}^{-1}$.

3.2. *Sample Preparation*

Solid samples were cut out of monocrystals which were prepared in the NIRIM at Tsukuba by Czochralski's pulling method from $LiNbO_3$ rods obtained by sintering. The Li_2CO_3 and Nb_2O_5 powders of high purity (99.99%) and natural isotopic abundance were mixed in congruent composition and calcined at 1273 C for 5 hours. The lamella are thinned by polishing until their weight agrees with the wanted thickness of the liquid samples. Two samples were studied at decreasing temperatures; the first one, E_I, at ten different temperatures, in the T-range $1673\ \mathrm{K} \geq T \geq 1518$ K; the second one, E_{II}, at six different temperatures between 1626 and 1513 K (the lower temperature limit depending on the depth of the undercooling domain which was reached). During these experiments, the thickness of the sample varied from 144 μm to 80 μm for E_I and from 46 μm to 35 μm for E_{II}.

4. Results

4.1. *Reciprocal Space Representation*

The curves of coherent intensity expressed in relative units, $I(k)$, are shown in Figure 4. For $T \leq 1553$ K, the intensity rises sharply as k goes to zero. The poor accuracy obtained in region $\{1\}$ is due to low counting rate, limited number of experimental points and high parasitic air scattering not easily suppressed between

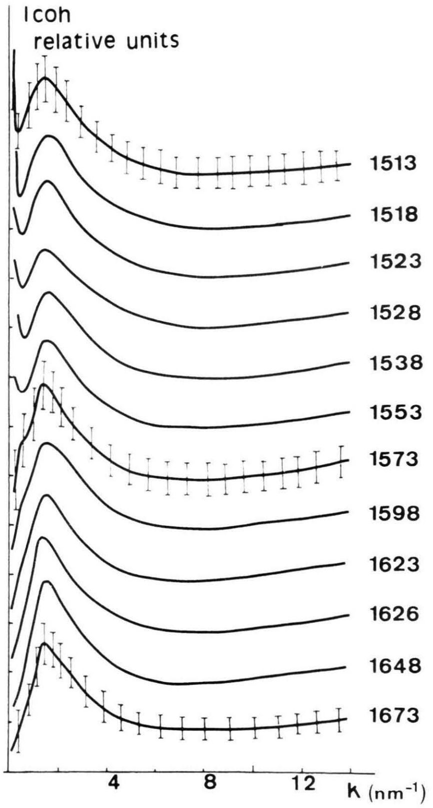

Fig. 4. Experimental coherent intensity, expressed in relative units, versus k; $I_{\mathrm{coh}}(k)$ at various temperatures, expressed in degrees K (error bars are given)

0.20 nm^{-1} and 0.05 nm^{-1}. The radius of gyration, R_g, obtained from Guinier's approximation applied in region {1} and the mean radius of gyration, R_{0m}, obtained from the results of region {2} are plotted in Figs. 5 and 6, respectively. The large difference between the values R_g and R_{0m} indicates that two kinds of particles are present in the melt, near freezing. The small ones, which we refer to as microclusters, show sizes with a weak temperature dependence, but the large ones, named macroclusters, have a size which rapidly increases as T goes down to the freezing point. The mean size "a" and correlation length l_c relative to the small clusters are also plotted in Figure 6. Their average distance $\bar{d}$ is shown in Figure 7. The error $\Delta\Theta_m \approx \pm 0.02°$ in the Θ_m evaluation from the unsymmetrical interference peak is the main cause of the high inaccuracy $\Delta\bar{d} \approx \pm 0.125$ nm. For $T > 1600$ K, the linear increase of $\bar{d}$ with T becomes 0.24×10^{-4} nm K^{-1}, a value corresponding exactly to a third of the relative density variation measured by Shigematsu et al [2]. This confirms a weak change in the size and number of microclusters. The linear evolution disappears for $T \leq \approx 1600$ K, and an anomalous behaviour is observed centred at $T \approx 1555$ K. Changes in size, shape or number of clusters have to be considered around this temperature. The large scatter, observed in $\bar{d}$, could also be due to this cluster rearrangement. The particle parameters, such as the volume v_p and the cross section A_{csp}, determined from the relations of Porod using the limits of $\{I(k)\}_{k\to 0}$, $\{k \cdot I(k)\}_{k\to 0}$, and $\{k^2 \cdot I(k)\}_{k\to 0}$, are reported Table 1.

Table 1. Parameters of the clusters: volume v_p (nm^3) and cross section A_{csp} (nm^2) deduced from the limits $I(k)_{k\to 0}$, $k \cdot I(k)_{k\to 0}$ and $k^2 \cdot I(k)_{k\to 0}$ using the Porod's formula [12]. The accuracy is ≈10% for these determinations.

T(K)	v_p	A_{csp}
1673	0.09	0.12
1648	0.23	0.15
1626	0.43	0.52
1623	0.44	0.54
1598	0.44	0.53
1573	0.45	0.52
1553	0.45	0.56
1538	0.94	0.61
1528	1.44	0.67
1523	2.30	0.81
1518	2.49	0.94
1513	3.20	1.50

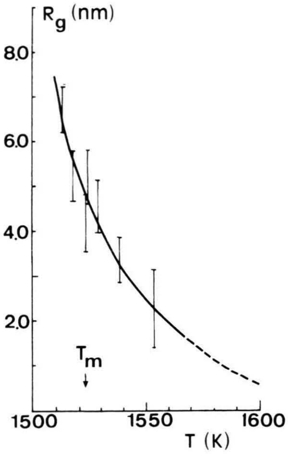

Fig. 5. Evolution of the radius of gyration of the macroclusters versus T; $R_g(T)$, R_g is deduced from Guinier's approximation [11].

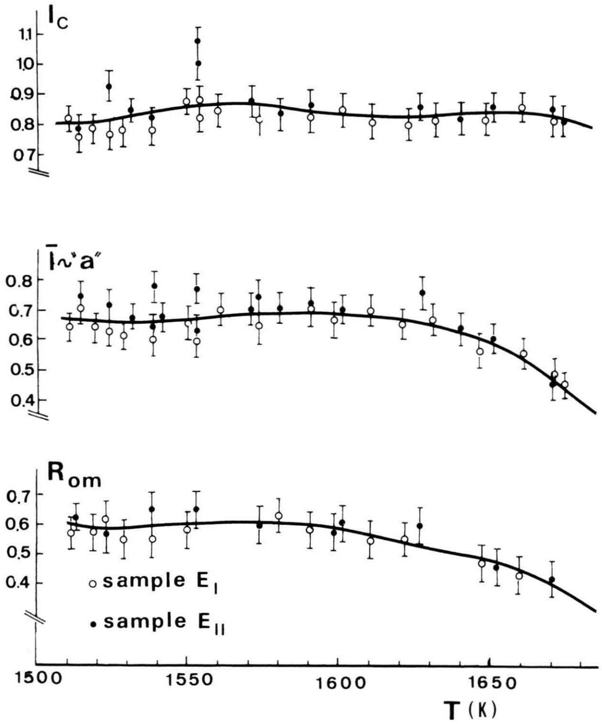

Fig. 6. Parameters (in nm) of the microclusters related to the interference effect. R_{0m} = mean radius of gyration, evaluated by the Hosemann's method [16]. "a" = mean size, evaluated from the Δk width of the interference peak. l_c = extent of coherence evaluated by the Porod's method [12] (the solid line is the least squares polynomial fit of the sixth order).

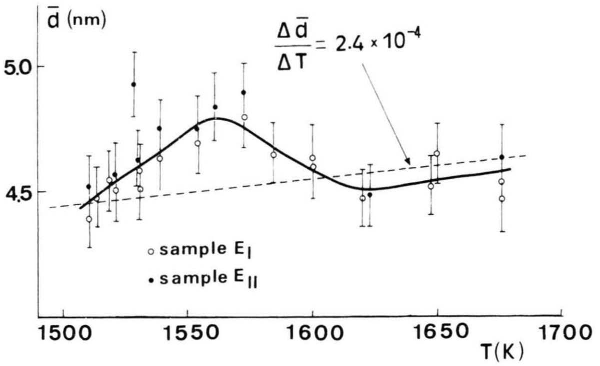

Fig. 7. Evolution of the average distance between the microclusters versus T; $\bar{d}$ is evaluated from the Ehrenfest method [15], the solid line is the least squares polynomial fit of the sixth order, the dashed line corresponds to a linear increase of $d(T)$.

4.2. *Real Space Representation*

Because of the parasitic ripples appearing in the curve $p(r)$ obtained from the Fourier transformation of the data using the experimental limit $k_{\max}$ for integration, a second transformation was made using the curve extended up to $150\ \mathrm{nm}^{-1}$. The supplementary data were obtained by computing the theoretical scattering due to spherical microclusters having a radius of gyration $R_{0\mathrm{m}}$ (value estimated from the peak of interference at each temperature). The contrast $\Delta\varrho$ is assumed equal to the difference between the electron densities of the solid $\mathrm{LiNbO_3}$ at T_m and the melt at the considered temperature. By this artificial extension, the termination ripples were suppressed while the real peaks were slightly altered. Nevertheless, the trend of the peaks, observed in the functions $p(r)$ and $f(r)=p(r)/r$ (Figs. 8 and 9), was only used to find the

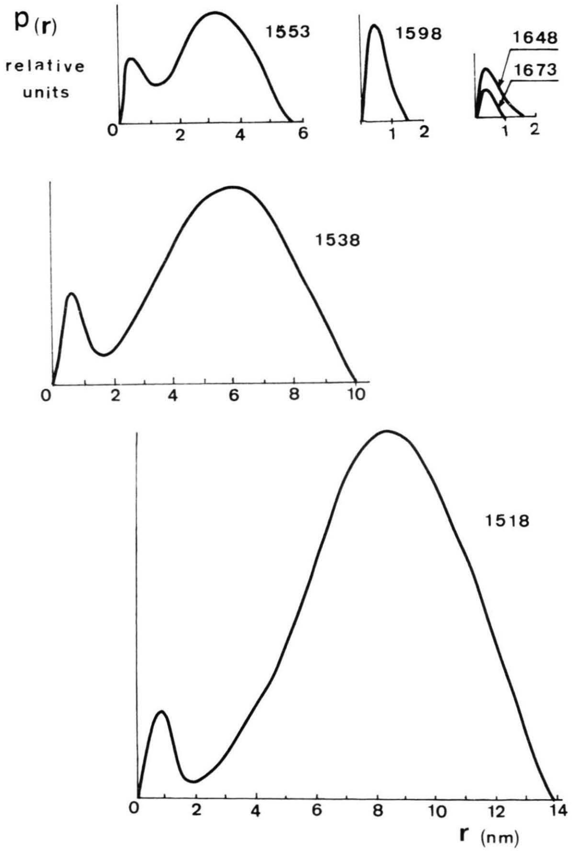

Fig. 8. Distance distribution function $p(r)$ plotted at different temperatures (T in degrees K).

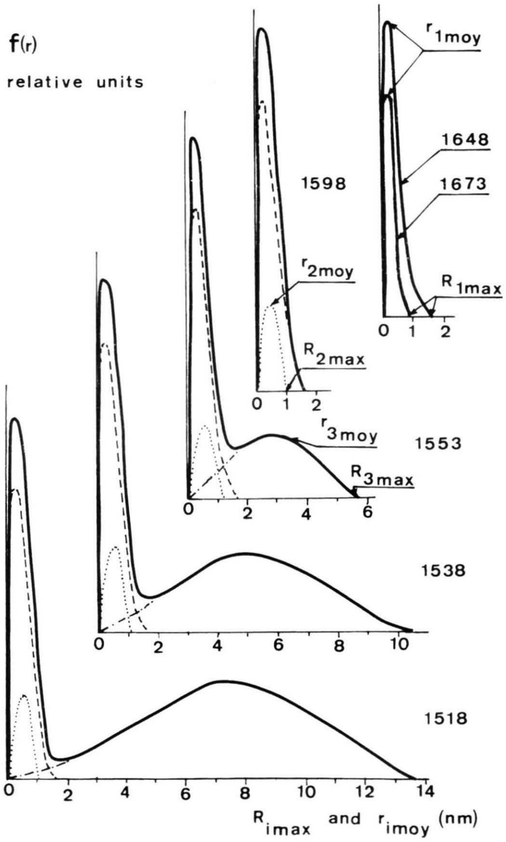

Fig. 9. Functions $f(r)=p(r)/r$, potted at different temperatures (expressed in degrees K); experimental curves (—); assumed contributions: chain (- - -), spherical microclusters (· · ·) and macrocluster (- · -); the values r_{imoy} and R_{imax} are determined with an accuracy of 10%.

class of possible cluster models [12, 13, 16]. The largest dimensions of the particles, deduced from these curves, are given by the *r* values where the peaks drop to zero in both functions. Only one peak is observed at the highest temperature. Its shape represents clusters having a length superior to the lateral sides (chains, rod-like particles or prolate ellipsoids). The length is given by $R_{1\mathrm{max}}$, the *r* value where this peak drops to zero, and the lateral side dimensions are obtained from the position of its maximum $r_{1\mathrm{moy}}$. On lowering the temperature, $R_{1\mathrm{max}}$ weakly increases while the maximum maintains its value $r_{1\mathrm{moy}}$. Then the peak is deformed, its maximum is weakly shifted to higher *r* values but a shoulder subsists on its left hand-side, always located at the same value $r_{1\mathrm{moy}}$. This evolution is clearly seen in the function $f(r)$. Its deformation is assumed due to the presence of two kinds of particles, so the peak is resolved into two contributions. The first one, assumed due to elongated particles, keeps the shape observed at 1648 K with the dimensions $R_{1\mathrm{max}}$ and $r_{1\mathrm{moy}}$. The second one, obtained after subtraction of the first one, has a shape corresponding to spheres of diameter $R_{2\mathrm{max}}$, the *r* value where this second component drops to zero. This assumption is consistent with the value $r_{2\mathrm{moy}}$ of its maximum since $r_{2\mathrm{moy}} \approx 0.525 \times R_{2\mathrm{max}}$, as it is described by Glatter et al. [13]. At $T \approx 1553$ K a broad peak appears on the right hand-side; it has been related to the quick aggregation of the particles. The increase in its area, the variation in its position and shape with the lowering *T* can be explained by the presence of spherical macroclusters with a diameter $R_{3\mathrm{max}}$, the *r* value where this peak drops to zero and the position of its maximum $r_{3\mathrm{moy}} \approx 0.525 \times R_{3\mathrm{max}}$. The values $r_{i\mathrm{moy}}$ and $R_{i\mathrm{max}}$ are plotted in Fig. 10 in terms of temperature. The shapes assumed and the size limits deduced from $p(r)$ and $f(r)$ are reported in Table 2. We have used these results only to choose the most probable descriptions amongst the cluster models obtained from the parameters previously determined in reciprocal space.

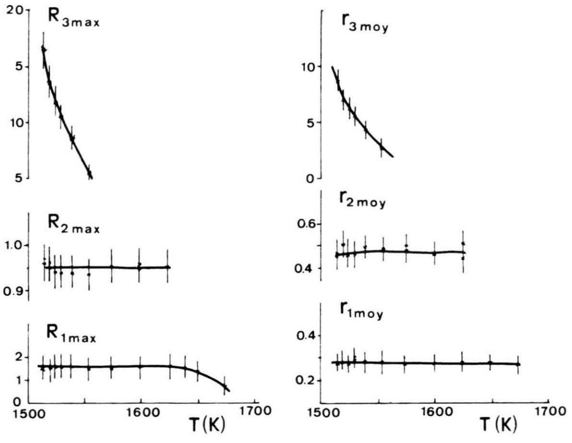

Fig. 10. Evolution of $r_{i\mathrm{moy}}$ and $R_{i\mathrm{max}}$ values (in nm) defined from the $f(r)$ functions versus *T*.

Table 2. Assumed shapes for the particles and their size limits (expressed in nm) deduced from the functions $p(r)$ and $f(r)$ in real space. The values $r_{i\mathrm{moy}}$ and $R_{i\mathrm{max}}$ are obtained with an accuracy of 10%.

T (K)	Cluster shapes and size limits			$r_{1\mathrm{moy}}$	$r_{2\mathrm{moy}}$	$r_{3\mathrm{moy}}$	$R_{1\mathrm{max}}$	$R_{2\mathrm{max}}$	$R_{3\mathrm{max}}$
	microclusters		macroclusters						
	1	2	3						
1673	chain 2 NbO_6	–	–	0.28			0.8		
1648	chain 2, 3 or 4 NbO_6	–	–	0.28			1.60		
1626	chain 2, 3 or 4 NbO_6	sphere $0.8 \leq \Phi \leq 1.0$	–	0.28	0.47		1.60	0.95	
1623	chain 2, 3 or 4 NbO_6	sphere $0.8 \leq \Phi \leq 1.0$	–	0.28	0.47		1.60	0.95	
1598	chain 2, 3 or 4 NbO_6	sphere $0.8 \leq \Phi \leq 1.0$	–	0.28	0.47		1.60	0.95	
1573	chain 2, 3 or 4 NbO_6	sphere $0.8 \leq \Phi \leq 1.0$	–	0.28	0.47		1.60	0.95	
1553	chain 2, 3 or 4 NbO_6	sphere $0.8 \leq \Phi \leq 1.0$	sphere $\Phi \approx 5.5$	0.28	0.47	2.80	1.60	0.95	5.5
1538	chain 2, 3 or 4 NbO_6	sphere $0.8 \leq \Phi \leq 1.0$	sphere $\Phi \approx 8.6$	0.28	0.47	4.40	1.60	0.95	8.6
1528	chain 2, 3 or 4 NbO_6	sphere $0.8 \leq \Phi \leq 1.0$	sphere $\Phi \approx 10.5$	0.28	0.47	5.70	1.60	0.95	10.5
1523	chain 2, 3 or 4 NbO_6	sphere $0.8 \leq \Phi \leq 1.0$	sphere $\Phi \approx 11.8$	0.28	0.47	6.20	1.60	0.95	11.8
1518	chain 2, 3 or 4 NbO_6	sphere $0.8 \leq \Phi \leq 1.0$	sphere $\Phi \approx 13.5$	0.28	0.47	7.00	1.60	0.95	13.5
1513	chain 2, 3 or 4 NbO_6	sphere $0.8 \leq \Phi \leq 1.0$	sphere $\Phi \approx 17.0$	0.28	0.47	8.70	1.60	0.95	16.5

5. Discussion

5.1. *Microcluster Models*

The interference patterns confirm the presence of microclusters in the whole temperature domain explored in this work. Models are built using NbO_6 octahedra since in this temperature range it was verified previously [7, 8] that Nb is octahedrally coordinated. In the melt, the clusters are probably built in a way similar to that of the dense paraelectric phase just before melting. The corner-sharing NbO_6 octahedra display a regular periodic sequence of Li and Nb atoms. This distribution can be reproduced locally by chains of octahedra, by ReO_3-type slabs [26] constituted by chains laterally linked in the same plane, and by regular or deformed elementary blocks built with two slabs of $(2 \times 2 \times 1)$ NbO_6 octahedra interlocked by a Li atom (see Figures 1 and 11). These simple forms are matched with geometric forms such as cylinders, ellipsoids, lamella, prisms and spheres, respectively, whose parameters can be computed and compared with the experimental values R_{0m}, "a" and l_c. The retained shapes are selected on the basis of the agreement between computed and experimental values. Taking into account the maximal dispersion observed for the value of l_c at $T = 1553$ K, we have retained all the models in which $l_c \leq 1.1$ nm. At $T = 1673$ K, microclusters have therefore been described in their simplest forms as dimers of NbO_6 octahedra. Below $T = 1648$ K, chains of at most three or four octahedra (the number of octahedra in the chain being limited by the experimental value $\overline{l}$) and slabs of $(2 \times 2 \times 1)$ octahedra could be present. At 1626 K, blocks of $(2 \times 2 \times 2)$ octahedra and slabs of $(3 \times 2 \times 1)$ octahedra could appear and subsist down to freezing. These results are compared with those deduced from Porod's law, reported in Table 1, and with those obtained in real space, reported in Table 2. From 1626 K to 1553 K, the average section of the scattering particles, A_{csp}, remains constant and equal to $\approx 0.55 \pm 0.05$ nm^2, their mean volume, v_p, is also constant and equal to $\approx 0.44 \pm 0.05$ nm^3. These values are in good agreement with the section and the volume of a block of $(2 \times 2 \times 2)$ octahedra. The evolution of A_{csp} and v_p, observed for $T \leq 1553$ K could be explained by the presence of the large clusters at low temperatures. The values of thickness deduced from Porod's law do not agree with the r_{1moy} values obtained in real space, and the lamella shape does not correspond to the forms (rod, regular prism or sphere) deduced from the components of $f(r)$. So the slabs were not retained in this work.

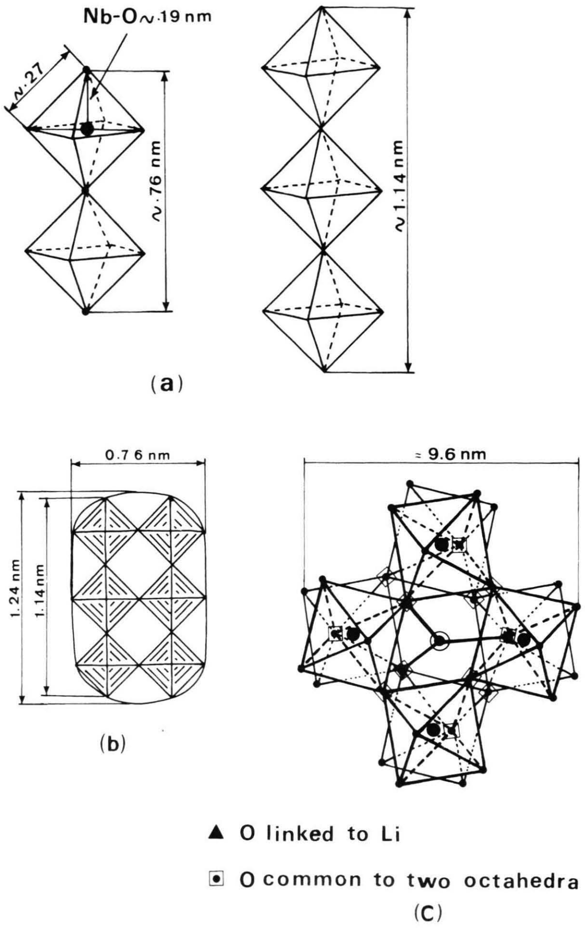

Fig. 11. Possible forms of microclusters. a) chains of two and three NbO_6 octahedra, b) slabs of $(3 \times 2 \times 1)$ NbO_6 octahedra, c) deformed block of $(2 \times 2 \times 2)$ NbO_6 octahedra.

5.2. *Cluster Evolution*

The number of microclusters, n_{mc}, is evaluated from the $\overline{d}$ value. For instance at 1626 K, this number is $n_{mc} \approx (109 \pm 9) \times 10^{17}$ cm^{-3}. The evolution of $I(k)_{k \to 0}$ and the non linear temperature dependence of $\overline{d}$ were explained by a regrouping of microclusters. At the onset of macroclustering, the number of macroclusters, N_{Mc}, consisting of a few microclusters, is assumed large enough to give a perceptible interference effect seen as a shoulder on the left hand-side of the interference peak. By lowering the temperature, the size of these large particles probably increases by regrouping, their number decreases, so their interference effect is wiped out, but at the same time their contribution appears as the rise of the curves for $k \Rightarrow 0$.

This correlates with the anomalous rise of viscosity [1–3] below 1553 K (see Figure 12). Such deviations of viscosity, at the approach of a freezing point, were explained by Ubbelohde [27] as a "clustering" in the melt. At any temperature, T_i, the viscosity, η_i, may be written in the form of a series expansion in powers of the cluster volume fraction, Φ_i, as

$$\eta_i/\eta_0 = 1 + \alpha\,\Phi_i + \beta\,\Phi_i^2 + \ldots, \tag{13}$$

where η_0 is the viscosity of the medium at T_i in the absence of any clusters [28]. For Φ_i not exceeding about 0.3, the series may be terminated at the third term with $\alpha \approx 2.5$ for spheres (≈ 2.0 for rods) and $\beta \approx 7.0$. The viscosity follows the exponential relation of Arrhenius, and the viscosity-temperature relationship is given by

$$\log \eta = A + B/T, \tag{14}$$

where A, depending on η_0, is inversely proportional to the cluster volume, and B has the properties of an activation energy. These values are accessible by experiments when the Arrhenius behavior is observed in a sufficiently, large T-domain above T_m. The results obtained by Shigematsu et al. [2] are reported in Table 3. Assuming that the sharp increase of η, observed at 1553 K, is only due to the "macroclustering", these authors have estimated the mean macrocluster volume as 74 nm^3 at this temperature (that is to say a volume equivalent to a sphere of radius $r_s \approx 2.6$ nm and constituted by $\approx 1682 \pm 10$ elemenatry blocks of $(2 \times 2 \times 2)$ octahedra). Their estimation of the size of clusters is reported in Table 4, together with our ones deduced from the experimental values R_g assuming spherical aggregates. At 1553 K, a difference $\Delta v_{Mc}/v_{Mc} \cong 20\%$ is observed between the macrocluster volumes evaluated from the two approaches.

Table 3. Viscosity data measured by Shigematsu et al. [2]. The volume fraction of clusters, Φ_i, is deduced from the η_i and η_0 values through (13). The first two values are obtained on the extrapolated curves.

T (K)	Viscosity ($\times 10^{-2}$ poise)		Φ_i (in %) Volume fraction of clusters
	η_i	η_0	
Extrapolated data			
1673	4	4	0
1648	10	10	0
Measured data			
1626	19	18.9	0.4
1623	22	21.7	0.5
1598	38	37.5	0.6
1573	45	43.9	1.0
1553	60	57	2.0
1538	75	64	6.0
1533	85	67	8.5
1528	101	69	13.5
1526	109	70	15.5
1523	118	71	17.7
1518	128	72	20.0
1513	150	76	23.5

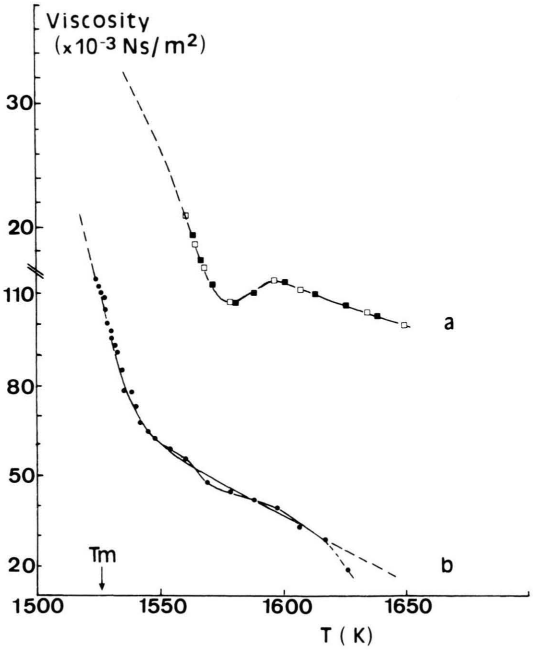

Fig. 12. Variation of viscosity versus T; $\eta(T)$. a) kinematic viscosity measured by Bol'shkov et al. [1] as a function of temperature during heating and cooling after holding for 25–30 min. To establish the kinematic viscosity, the authors determined the logarithmic damping decrement and torsional oscillation period of the crucible in the melt. b) viscosity measured by Shigematsu et al. [2] using a Pt sphere balance viscometer. The time required to move the sphere in the melt is measured by a stopwatch and the viscosity calculated from this time, referring to the calibration curve which was obtained by a measurement of silicon oil of known viscosity.

5.3. Evaluation of Cluster Numbers

With some simplifying assumptions it is possible to deduce roughly the number of clusters present in the melt at T_i from the Φ_i and R_g values. For this, we assumed cylindrical shape for the chains and spherical

Table 4. Experimental values of R_g (nm), the radius of gyration of the macroclusters, versus temperature. The parameters of particles: radius r_s (nm), Volume v_{Mc} (nm^3) and surface s_{Mc} (nm^2) are calculated for spherical macroclusters. The values in brackets are obtained by Shigematsu et al. [2].

T (K)	R_g	Radius r_s	Average volume v_{Mc}	Average surface S_{Mc}
Extrapolated data				
1598	0.8	1.0	4.6	13.4
1573	1.4	1.8	24.7	47.1
Measured data				
1553	2.2 ± 0.6	2.8 ± 0.8 $\{2.6\}$	92 $\{74\}$	1.0×10^2 $\{0.9 \times 10^2\}$
1538	3.2 ± 0.6	4.1 ± 0.8	290	2.1×10^2
1533	3.7 ± 0.6	4.8 ± 0.8	463	2.9×10^2
1528	4.2 ± 0.6	5.4 ± 0.8	660	3.7×10^2
1526	4.4 ± 0.6	5.6 ± 0.8	756	3.9×10^2
1523	4.6 ± 0.6	5.9 ± 0.8	860	4.4×10^2
1518	5.2 ± 0.6	6.7 ± 0.8	1260	5.6×10^2
1513	6.8 ± 0.6	8.8 ± 0.8	2850	9.7×10^2

shape for the blocks (2 × 2 × 2) octahedra and for the macroclusters. At 1673 K and 1648 K, the microclusters are described as chains of 2 and 3 NbO_6 octahedra for which the volumes are ≈ 0.09 and ≈ 0.13 nm^3, respectively. For these two temperatures, the behaviour of the viscosity ($\eta_i = \eta_0$) corresponds to the one of a liquid without any cluster with Φ_i equal to 0%, although the computed total volume of chains corresponds to Φ' equal to 0.09 and 0.13% of the sample, respectively. This fact is explained by assuming that the small chains have no real influence on the viscosity in this T-range. Therefore from 1626 K, we have neglected the chains due to this observation. Only the blocks of (2 × 2 × 2) NbO_6 octahedra are retained to describe the small clusters. With this assumption, the volume of microclusters, given by $V_{mc} = n_{mc} \cdot v_{mc}$ appears approximately constant with v_{mc}, the volume of small blocks (2 × 2 × 2) NbO_6, evaluated as ≈ 0.44 nm^3. But from 1626 K to 1553 K, the experimental Φ_i value weakly increases. At 1626 K the negative deviation ($\Phi_i - \Phi'$) was explained by the presence of some chains (about 25% of n_{mc}). At 1623 K, the values Φ_i and Φ' are in good agreement. Then at 1598 K and 1573 K, the deviation becomes positive; it was explained by the progressive beginning of macroclustering observed as a shoulder on the SAXS curves. For these two temperatures Guinier's approximation cannot be applied, also the volume of a macrocluster is evaluated using the extrapolated R_g values (see Fig. 5 and Table 4). Their number, N_{Mc}, is deduced from Φ_i as $N_{Mc} = (100\ \Phi_i - V_{mc})/v_{Mc}$, assuming $\Phi' = \Phi_i$. This method is always applied for $T \leq 1553$ K, with the volume v_{Mc} calculated from the experimental radius of gyration R_g. The rough number of small blocks, n_b, contained in a macrocluster is given by $n_b \approx v_{Mc}/v_{mc}$, assuming "macroclustering" due to a regrouping of small blocks. These results, normalized to 1 cm^3, are reported in Table 5, and their evolution versus T is shown in Figure 13. On further cooling, the macrocluster size increases rapidly, and the sharp viscosity change might be caused by these large aggregates. In the undercooling domain the rapid decrease of N_{Mc} could be due to a formation of very large aggregates as crystalline embryos.

A control of our assumptions is obtained by computing the total area, S_{Total}, of scattering particles. The computed specific surface per unit volume, $S_{sp2} = S_{Total}/V_{sample}$, is then compared to the experimental specific surface, S_{spl}, related to the limit $\{k^4 I(k)\}$ through (6). The product $k^4 I(k)$ remains constant over a reasonable k-interval only at few temperatures. The S_{spl} values are computed with the density contrast, $\Delta\varrho$, evaluated assuming a cluster density equal to the crystalline one extrapolated to the appropriate temperature. On account of errors made in density and viscosity measurements, these determinations were obtained with an accuracy of ±20%. For instance at 1523 K,

Table 5. Number of clusters in 1 cm^3 of melt. n_{mc} and N_{Nc}: numbers of micro- and macroclusters, respectively. n_b: number of blocks of (2 × 2 × 2) NbO_6 octahedra in a macrocluster. V_{total}: total volume of clusters (nm^3). Φ_{imc} and Φ_{iMc}: volume fractions of the micro- and macroclusters, respectively.

T (K)	N_{Mc} $\times 10^{17}$	n_b	n_{mc} $\times 10^{17}$	V_{Total} $\times 10^{17}$	Φ' in % = $\Phi_{imc} + \Phi_{iMc}$
1673			100 ± 8	9	0.09
1648			103 ± 8	13.4	0.13
1626			109 ± 8	48.0	0.48
			75% blocks	36.0	
			+	+	0.40
			25% chains	4.0	
1623			105 ± 8	46.2	0.46
1598			105 ± 8	44.9	0.45
extrapolated	3.2	32	105 ± 8	44.9	0.45 + 0.15
1573			109 ± 9	47.9	0.48
extrapolated	2.2	69	109 ± 9	47.9	0.48 + 0.52
1553	1.71	210	98 ± 12	200.0	0.43 + 1.57
1538	1.93	660	90 ± 12	600.0	0.40 + 5.60
1528	1.98	1500	99 ± 10	1350.0	0.44 + 13.06
1526	1.99	1720	98 ± 10	1550.0	0.43 + 15.07
1523	2.01	1955	96 ± 10	1770.0	0.42 + 17.28
1518	1.55	2865	109 ± 10	2000.0	0.48 + 19.52
1513	0.81	6475	104 ± 10	2350.0	0.46 + 23.04

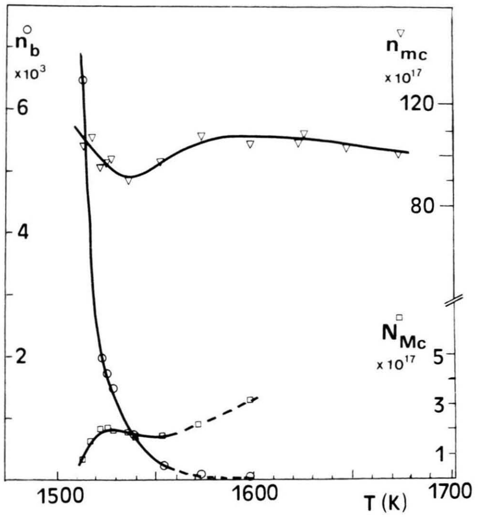

Fig. 13. Evolution of the number of micro- and macroclusters in one cm^3 of melt versus T; n_{mc} (▿): number of microclusters, N_{Mc} (□): number of macroclusters, n_b (○): number of blocks of (2 × 2 × 2) NbO_6 in a macrocluster.

Table 6. Limit of the normalized product $k^4 \cdot I(k)$. The specific surface S_{sp1} is obtained from the limit $k^4 \cdot I(k)$. The surface S_{Total} (nm^2) is computed with macroclusters and small blocks. The values S_{sp1}, S_{sp2} and their difference $\Delta S_{sp(1-2)}$ are expressed in nm^{-1}.

T(K)	Limit $k^4\,I(k)$	S_{sp1} (nm^{-1})	S_{Total} $S_{micro}+S_{macro}$ (nm$^2 \times 10^7$)	S_{sp2} (nm^{-1})	$\Delta S_{sp(1-2)}$
1553	0.054 ± 0.006	0.036 ± 0.008	227 + 171	0.040	−0.004
1538	0.041 ± 0.004	0.075 ± 0.015	208 + 405	0.061	+0.014
1523	0.030 ± 0.003	0.115 ± 0.023	223 + 884	0.111	+0.004
1518	0.023 ± 0.003	0.111 ± 0.022	253 + 868	0.112	−0.001

we obtain $\Delta\varrho \approx 3.4 \pm 0.5$ atoms · nm^{-3} with $\Delta\varrho_{cluster} \approx 17.7 \pm 0.2$ atom · nm^{-3} and $\Delta\varrho_{matrix} \approx 14.3 \pm 0.3$ atom · nm^{-3}; this last value is obtained with the density of the liquid matrix deduced from the melt density data [2] after correction to take the presence of clusters into account as $d_{matrix} = (d_{melt} - \Phi_i \cdot d_{cluster})/(1 - \Phi_i)$. The values ΔS_{sp1}, S_{sp2} and their difference $\Delta S_{sp(1-2)} = S_{sp1} - S_{sp2}$ are reported in Table 6. The deviation is always included in the error limits.

The results obtained from different determinations are in good agreement. Nevertheless, the numbers of clusters can be contested since we have to make assumptions on the shapes and the electronic density of the scattering particles.

6. Conclusion

The study of liquid $LiNbO_3$, using SAXS, has shown that microclusters are present in the liquid below 1673 K and subsist down to freezing. Chains and blocks formed by corner sharing NbO_6 octahedra have been suggested to describe these microclusters. Below 1575 K, macroclustering appears to result from a re-arrangement of the microclusters. The sharp increase of the viscosity could be explained by the volume fraction of clusters in the melt. For each temperature the number and volume fraction of clusters has been obtained from a combination of SAXS and conventional viscosity data. The limits of precision are unambiguously reported. Taking the low accuracy of high temperature experiments into account, our data can seem over interpreted. Nevertheless these results, obtained from an original method, give a possible explanation of the evolution of the melt structure near solidification. We conclude that SAXS results, connected with viscosity measurements, are a very effective tool to study clustering and nucleation in the domain of precrystallization.

Acknowledgements

The samples were prepared in the NIRIM, and the SAXS experiments were carried out at the Photon Factory of KEK at Tsukuba (Japan). The data were analysed using the computer facilities of CNRS at Bellevue (France). The authors wish to thank the members of these laboratories for their effectual support. They are specially grateful to Prof. Y. Waseda of Tohoku University for making this collaboration possible, to Prof. Y. Inoko of Osaka University for his help in the beam line arrangement and to Dr. P. Chieux of ILL (Grenoble France) for helpful discussions. One of the authors P.A. owes this work to STA financial support (Science & Technology Agency fellowship) from the JISTEC (Japan International Science and Technology Exchange Center). This work was also supported by the Special Coordination Fund for Promoting Science.

[1] S. A. Bol'shkov, V. P. Klyuev, N. N. Lyapushkin, A. P. Lyubimow, and S. A. Fedulov, Inorg. Mater (USSR) **5,** 824 (1969).

[2] K. Shigematsu, Y. Anzai, S. Morita, M. Yamada, and H. Yokoyama, Japan J. Appl. Phys. **26,** 1988 (1987).

[3] J. A. S. Ikeda, V. J. Fratello, and C. D. Brandle, J. Cryst. Growth **92,** 271 (1988).

[4] N. Niizeki, T. Yamada, and H. Toyoda, Japan J. Appl. Phys. **6,** 151 and 318 (1967).

[5] Y. S. Luh, R. S. Feigelson, M. M. Fejer, and R. J. Byer, J. Cryst. Growth **78,** 135 (1986) and **85,** 264 (1987).

[6] A. A. Ballman, J. Amer. Ceram. Soc. **48,** 112 (1965).

[7] K. Sugiyama, K. Nomura, Y. Waseda, P. Andonov, S. Kimura, and K. Shigematsu, Z. Naturforsch. **45a,** 1325 (1990).

[8] P. Andonov, P. Chieux, and S. Kimura, J. of Phys: Condensed Matter **5,** 1 (1993).

[9] S. C. Abrahams, J. M. Reddy, and J. L. Bernstein, J. Phys. Chem. Solids **27,** 997 (1966). S. C. Abrahams, W. C. Hamilton, and J. M. Reddy, J. Phys. Chem. Solids **27,** 1013 (1966). S. C. Abrahams, H. J. Levinstein, and J. M. Reddy, J. Phys. Chem. Solids **27,** 1019 (1966).

[10] H. Boysen and F. Altorfer, Acta Cryst. **B50,** 405 (1994).

[11] A. Guinier and G. Fournet, Small-Angle Scattering of X-rays, Wiley, New York 1955.

[12] G. Porod, Kolloid. Z. **124,** 83 (1949); **125,** 51 and 109 (1952); Small-Angle X-ray Scattering, Proceedings of the Conference held at Syracuse University 1965 editor H. Brumberger.

[13] O. Glatter and O. Kratky, Small Angle X-ray Scattering, Academic Press Inc., London 1982.

[14] N. W. Ashcroft and J. Lekner, Phys. Rev. **145,** 83 (1966).

[15] R. Ehrenfest, Proc. Amsterdam Acad. **17,** 1132 and 1184 (1915).

[16] R. Hosemann and S. N. Bagghi, Direct Analysis of Diffraction Matter, North-Holland Publishing Company, Amsterdam 1962.

[17] D. T. Cromer and J. T. Waber, Acta Crystallogr. **18,** 104 (1965).

[18] D. T. Cromer, Acta Crystallogr. **18,** 17 (1965).

[19] International Tables of X-ray Crystallography, Kynock-Press, Birmingham 1962.

[20] K. Sagel, Tabellen zur Röntgenstrukturanalyse, Springer-Verlag, Berlin 1958.

[21] B. E. Warren, X-ray Diffraction, Addison-Wesley Publishing Company Inc., Massachusetts 1969.

[22] G. Malet, C. Cabos, A. Escande, et P. Delord, J. Appl. Crystallogr. **6,** 139 (1973).

[23] R. T. Smith and F. S. Welsh, J. Appl. Phys. **42,** 2219 (1971).

[24] M. Abramowitz and I. A. Stegun, Handbook of Mathematical Functions with Formulas, Graphs and Mathematical Tables, U.S. National Bureau of Standards Applied Mathematics, Series 55, Washington 1964.

[25] V. Luzzati, Acta Crystallogr. **13,** 939 (1960).

[26] A. F. Wells, Structural Inorganic Chemistry, fifth edition, Clarendon Press, Oxford 1986.

[27] A. R. Ubbelohde, The Molten State of Matter, **C13,** John Wiley, New York 1977.

[28] E. McLaughlin and A. R. Ubbelohde, Trans. Faraday Soc. **54,** 1804 (1958) and **56,** 988 (1960).